SAND2000-0859J

March 10, 2000

Control of the Interparticle Spacing in Gold Nanoparticle Superlattices

James E. Martin, Jess P. Wilcoxon, Judy Odinek, and Paula Provencio

Sandia National Laboratories

Albuquerque, New Mexico 87185-1421

Abstract

We have investigated the formation of 2-D and 3-D superlattices of Au nanoclusters synthesized in nonionic inverse micelles, and capped with alkyl thiol ligands, with alkane chains ranging from C_6 to C_{18}. The thiols are found to play a significant role in the ripening of these nanoclusters, and in the formation of superlattices. Image processing techniques were developed to reliably extract from transmission electron micrographs (TEMs) the particle size distribution, and information about the superlattice domains and their boundaries. The latter permits us to compute the intradomain vector pair correlation function, from which we can accurately determine the lattice spacing and the coherent domain size. From these data the gap between the particles in the coherent domains can be determined as a function of the thiol chain length. It is found that as the thiol chain length increases, the nanoclusters become more polydisperse and larger, and the gaps between particles within superlattice domains increases. Annealing studies at elevated temperatures confirm nanocluster ripening. Finally, the effect of the particle gaps on physical properties is illustrated by computing the effective dielectric constant, and it is shown that the gap size now accessible in superlattices is rather large for dielectric applications.

Sandia is a multiprogram laboratory operated by Sandia Corporation, a Lockheed Martin Company, for the United States Department of Energy under contract DE-AC04-94AL8500. This work supported by the Division of Materials Sciences, Office of Basic Energy Sciences, U.S. Department of Energy (DOE).

DISCLAIMER

Introduction

There has been considerable recent interest in the formation of superlattices of metal nanoclusters synthesized by solution or gas phase methods. Here we report the synthesis of superlattices of unfractionated Au nanoclusters made in inverse micelle solutions using a family of nonionic surfactants with polyether headgroups. The goal of these studies is to test methods of controlling the interparticle spacings in these superlattices, and to determine the range of interparticle spacings that can be achieved. Some transport properties, such as tunneling currents, are exponentially dependent on particle spacings, whereas others, such as the dielectric and electrostrictive coefficients, depend algebraically on the particle gaps, as we illustrate below. Control of the gaps is an important aspect of developing materials applications.

To investigate the issue of gap control, we capped the Au nanoclusters with alkanethiols having a range of chain lengths. We found that many, but not all, of these thiols facilitate superlattice formation. However, a number of unexpected parameters affect the results, including amount of time between reduction and capping, the choice of oil used to form micelles, the specific reducing agent, etc. To quantify the gaps between particles we developed image processing techniques that can compute a variety of parameters from TEM images of 2-D particle arrays. In addition to the particle size distribution, particles are classified as to whether or not they are in an ordered domain, and the crystalline domains are enumerated so that the coherent intradomain vector pair correlation function can be computed. This provides a precise determination of the lattice spacing and the coherence length in the superlattices, and combining this with the average particle size allows a precise determination of the particle gaps, which do indeed increase with the alkane thiol chain length.

Finally, a simple calculation of the dependence of effective dielectric constant as a function of particle gap is given, and it is shown that the dependence on the particle gap is strong. Possible applications of these materials to supercapacitors are considered.

The history of the surfactant-based synthesis of metal nanoclusters starts with the seminal 1982 paper of Boutonnet, Kizling, Stenius, and Maire,[1] who used two inverse micelles forming systems: 1) the nonionic surfactant penta(ethyleneglycol) dodecyl ether

in hexane and; 2) the cationic surfactant cetyl trimethylammonium bromide (CTAB), in octanol. The metal salts used were H_2PtCl_6, $PdCl_2$, $RhCl_3$, and $IrCl_3$, these metals being chosen for their catalytic potential. The successful preparations of Pt nanoclusters are illustrative. In the cationic surfactant case, the inverse micelles were swollen with a dilute, ~ 8 mM aqueous H_2PtCl_6 solution, to form inverse microemulsions with aqueous phase loadings of about 14 wt%. In the nonionic surfactant case, the inverse micelles were swollen with a concentrated, ~ 1.2 M aqueous H_2PtCl_6 solution, to form inverse microemulsions with aqueous phase loadings of about 0.3 wt% and Pt ion concentrations of 4 mM. These precursor solutions were then reduced with hydrazine to form a stable dispersion of ~3 nm diameter Pt nanoclusters.

The use of water restricts the synthesis of metal nanoclusters to inert metals which are not easily oxidized. In 1989 it was demonstrated[2,3] that the synthesis of metal nanoclusters could be done in inverse micelle solutions, by directly dissolving the metal salt into an oil containing certain types of surfactants which spontaneously aggregate to form droplet-like micelles with nanometer dimensions and hydrophilic interior regions. This method was shown to give more monodisperse nanoclusters than those produced by a microemulsion synthesis using the nonionic poly(ethyleneglycol) alkyl ether surfactants. A typical synthesis uses the nonionic surfactant penta(ethyleneglycol) dodecyl ether in octane and the metal salt $NaAuCl_4$. This inverse micelle synthesis also permits the use of strong reducing agents, such as $LiBH_4$, which is hydrolyzed by water. Using this technique, nanoclusters of easily oxidizable metals, such as Fe, can be produced[4].

The first mention of the formation of Au nanocluster superlattices of which we are aware is in a 1993 paper by Giersig and Mulvaney[5], who synthesized Au nanoclusters by the aqueous Turkevich method[6], in which $AuCl_4^{-1}$ is reduced by sodium citrate. These 14 nm diameter, negatively charged clusters were deposited onto a TEM grid by application of a 10-100 mV potential, forming monolayer arrays of large extent. The gap between these particles was 1.0 nm, consistent with the size of the citrate ion stabilizer.

In 1994 Brust et al.[7] reported an inverse micelle synthesis of Au nanoclusters, but using the cationic surfactant tetraoctylammonium bromide in toluene. The method of salt

addition is not direct however, but is introduced into the toluene/surfactant phase by first dissolving the metal salt in water, then extracting the metal salt into the inverse micelle solution. This is a true inverse micelle synthesis, because water is not extracted into the organic phase, and in fact, use of the aqueous salt solution is unnecessary, since the metal salt can be directly dissolved into the inverse micelle solution. The reducing agent was aqueous sodium borohydride, and the clusters were capped with dodecanethiol. Dodecanethiol was introduced into the organic phase before reduction, to limit cluster growth and to stabilize the clusters. Brust later reported[8] the formation of superlattices of 8 nm Au nanoclusters crosslinked with dithiols, specifically, 1,12 dodecanedithiol and *p*-xylenedithiol.

Heath and co-workers[9] repeated the cationic inverse micelle synthesis, but varied the molar ratio of dodecanethiol to Au in an effort to control the nanocluster size, forming nanoclusters with a domain size over the range of 1.5 to 20 nm, as determined from the Debye-Scherr x-ray diffraction (XRD) linewidth. However, the reported optical absorption peak range of 520-545 nm is consistent with particle sizes greater than ~10 nm diameter in toluene. For example, for 5 nm diameter thiol-coated Au nanoclusters, the optical absorption maximum is at 505 nm, while for 2 nm clusters there is no absorption maximum[3,10]. From this one can conclude that >10 nm clusters consisting of several crystalline domains were formed. Whetten et al.[11] also repeated the cationic inverse micelle synthesis with higher dodecanethiol concentrations, in an effort to produce smaller nanoclusters, and successfully formed very nice 2-D and 3-D superlattices from ~2 nm thiol-coated nanoclusters. Heath and co-workers[12] later demonstrated the formation of superlattices from highly polydisperse dodecanethiol capped Au nanoclusters, and noted that the smaller clusters tended to segregate to the outside of the arrays, a result that is consistent with the simulations they report.

Andres et al.[13] demonstrated the formation of Au nanocluster superlattices, the clusters synthesized by a gas phase technique wherein the Au particles are stabilized by a dodecanethiol mist. The clusters formed conducting arrays when linked by aryl dithiols or aryl di-isonitriles. A number of other groups have formed superlattices of metal nanoclusters produced by coating with dodecanethiols[14-16], again using the inverse micellar synthesis technique. Dodecanethiol is chosen because of the good results it

gives in array formation. It has been our experience that preparing good superlattices from other chain length thiols is more difficult, requiring a preparation that produces very monodisperse nanoclusters.

To our knowledge, only one group has reported a study of the interparticle separation with metal nanoclusters functionalized with a family of ligands of variable chain length[17]. They employed the inverse micelle synthesis technique, using the tetraalkylammonium bromide ($NR_4^+Br^-$) family of cationic surfactants with R varying from C_6 to C_{18} in toluene[18]. An analysis of TEM images, using a graticule, gave a smaller than expected increase of 1.27 Å per carbon atom of the particle spacing on the chain length of the surfactant. It is mentioned that the cluster size distribution was affected by the choice of surfactant, but no analysis of the average cluster size was reported, so the effect of surfactant chain length on the particle gaps cannot be addressed.

In the following we report the synthesis and characterization of Au nanocluster arrays made with a range of thiol chain lengths, and focus on the complex role that alkyl thiols play in the stability and ripening of nanoclusters and their superlattices.

Experimental

Synthesis. We synthesize nanoclusters by an inverse micelle technique, in which the metal salt is directly dissolved into the inverse micelles without the addition of water. In this method, a 10 wt.% solution of an inverse micelle forming surfactant is first dissolved in an oil. The inverse micelle solution is added directly to the metal salt to prepare a solution that is 0.01M metal salt. This solution is protected from light and allowed to stir vigorously overnight to ensure complete dissolution of the salt. The chemical reduction of this precursor solution is then carried out in an oxygen- and moisture-free environment, in our case an argon filled Vacuum Atmospheres™ glovebox. The reducing agent is added with a pipette to the rapidly stirred solution to give a final concentration that is usually 0.04 M. The molar ratio of reducing agent to metal salt, *R*, and is listed in **Table I.** After removing the reacted solution from the glovebox, the clusters are stabilized by capping with an alkane thiol or other suitable capping agent at least one hour after chemical reduction - sometimes as long as one day or even one week.

The stable clusters could then be purified by various means. When the reagents and reaction conditions are appropriately selected, this method results in nearly monodisperse clusters that do not require fractionation to form superlattices with large domain sizes.

Surfactants. We use nonionic surfactants having a polyether headgroup attached to a linear hydrocarbon tail. These surfactants are designated by the nomenclature C_iE_j where i is the number of CH_x units in the alkyl chain and j equals the number of ether groups, e.g. $C_{12}E_5$ denotes penta(ethyleneglycol) mono n-dodecyl ether. In our syntheses i = 12 and j is in the range of 4 to 8. The ultrapure nonionic surfactants we use are obtained from Nikko chemicals, Japan. $C_{12}E_5$ is most often chosen, due to the ease with which it can be extracted into NMF.

Oils. A range of oils are used, including pentane, hexane, octane, decane, dodecane, and hexadecane. The oil is found to have an effect on the nanoparticle size and dispersity. The choice of oil used for a particular sample depends on the intended application of the nanoclusters. Pentane and hexane, because of their higher volatility, are used when samples are prepared for thin film applications. The long chain alkanes are chosen when formation of 2-d and 3-d arrays is the main focus. Nanocluster solutions of the alkanes decane or higher are more easily rendered ion free by extraction with deionized water, which is important for dielectric measurements, and tend to give the most stable Au nanoclusters, probably by reducing the alkane thiol lability.

Metal salts. We used a variety of metal salts to produce high quality Au nanoclusters. These are ammonium tetrachloroaurate (III) hydrate, hydrogen tetrachloroaurate (III) hydrate, and sodium tetrachloroaurate (III) hydrate. The choice of salt can be used to obtain some degree of size control.

Reducing agents. The reducing agents we use are lithium aluminum hydride, lithium aluminum hydride bis(tetrahydrofuran), lithium triamylborohydride (LS-Selectride®), lithium tri-*sec*-butylborohydride (L-Selectride®), lithium tris[(3-ethyl-3-pentyl)oxy]aluminohydride, lithium borohydride, and lithium triethylborohydride (Super-Hydride®). Gelation of the solution generally occurs when Au nanocluster solutions reduced with aluminum-containing compounds are extracted with n-methylformamide. Even if the surfactant is not extracted from these solutions, they will eventually gel. The choice of the reducing agent is a primary determinant in the quality of the nanoclusters.

Super-Hydride® consistently forms monodisperse nanoclusters, and though these are somewhat larger than those produced with $LiAlH_4$, they do not gel when the surfactant is extracted. Predilution of some of the reducing agents to 0.2 M with tetrahydrofuran or toluene caused a more rapid reaction upon addition into the metal salt solution, but then we often experienced problems upon extraction of the surfactant that could have been related to an excess of these diluents in the solution.

Annealing. During these studies it was discovered that aging the nanocluster solutions often leads to reduced polydispersity. Significant sample aging takes weeks or months, so we decided to determine whether thermal annealing could reduce this time. Several annealing experiments were tried. In one successful experiment an aliquot of **Au 494** (**Table I**) that had been at ambient temperature for 99 hours was annealed for 18 hours at 70° C and capped with dodecanethiol. Ordered 2-d superlattices were observed with TEM, forming by solvent evaporation on the holey carbon TEM grids. **Au 513** was prepared using different salt, oil, surfactant and reducing agent from that used in the preparation of **Au 494**, as shown in **Table I**. After 3 days at ambient temperature an aliquot of this sample was placed in a 70° C oven for 15 hours. A series of samples were prepared for TEM analysis by capping with thiols from hexanethiol to hexadecanethiol. The same series was later repeated with the parent **Au 513** sample that had been at ambient temperature for 32 days prior to capping with thiols, **Fig. 1**.

Purification. To purify the nanoclusters several approaches were used; liquid phase extraction, precipitation, and solid phase extractors. Before surfactant extraction from the inverse micellar solutions containing the nanoclusters, the nanoclusters are first rendered hydrophobic by capping the cluster surface with alkane thiols, designated C_kSH, where $3<k<18$ denotes the length of the alkyl group. Longer chain alkyl thiols, with $k\geq 8$, are the most effective.

Extraction. Liquid phase extraction is effective at removing the surfactant from samples prepared in simple alkanes, since alkanes are immiscible with the polar organic solvents in which the surfactants are highly soluble, while the alkane thiol capped nanoclusters are highly insoluble in polar solvents. This method has the advantage of keeping the nanoclusters dispersed throughout the process. To select effective extraction

solvents, the partitioning ratios of the surfactant between the polar and non-polar phases were determined for polar solvents, listed in **Table II** below, we found immiscible with the alkanes, (less polar solvents, such as ethanol, 1-propanol, 2-propanol and 2-butanol, form a reasonably stable emulsion with the inverse micelle solutions.) In these experiments 1.0 ml of the extracting solvent was added to 3.0 ml of a 1% surfactant in oil solution and the samples were vortex mixed. After the formation of two distinct phases, aliquots were removed from both phases and analyzed by high pressure liquid chromatography (HPLC) using the refractive index (RI) detector.

The efficacy of the extractants varied considerably, and it is interesting to note that the most likely extractant - water - is completely ineffective, as is MeOH, etc. However, n-methylformamide (NMF), with its extraordinarily high dielectric constant of 189, is very effective in extracting all the ionic by-products and most of the surfactant from thiol stabilized nanoclusters, even though the surfactant $C_{12}E_4$ has a relatively short polyether tail, compared to its long C_{12} alkane component. However, some NMF solubilizes into the alkane solvent, especially lower alkanes such as pentane. This residual NMF can be removed by extracting with water. In practice, the surfactant was removed by three extractions with NMF, the residual NMF is removed by three extractions with deionized water, and excess thiol capping agent is extracted with a 0.1 mM NaOH solution. The samples can be chilled and the oil phase decanted from the frozen water.

The surfactant partitioning ratio for decane/NMF system was then determined for a range of non-ionic surfactants with different size polyether chains, **Table III**. When the polyether chain exceeds E_4, the surfactant extraction is extremely efficient, and very few washes are required. This liquid phase extraction procedure is effective for a wide range of surfactants and metal nanoclusters.

Precipitation. An alternative and more conventional method of nanocluster purification is precipitation with a non-solvent. Precipitation of nanoclusters from solution by use of a non-solvent is effective for Au nanoclusters prepared in toluene. Unlike liquid extraction it cannot be used with nanoclusters prepared in high alkanes, since the polar, organic non-solvents like methanol, ethanol or acetone used to precipitate the hydrophobic alkane thiol stabilized Au nanoclusters from solution are immiscible in

alkanes. However, it is effective for removing surfactants from the solutions and results in good retention of the nanoclusters.

Precipitation does have its problems, however. In attempting to purify several Au samples with various chain length alkyl thiols a second time by MeOH precipitation, we discovered that excess purification washes the alkyl thiols off the clusters, leading to cluster aggregation, and even plating out of a Au film on the glass vial. We also found that the Au clusters do not precipitate a second time without aggressive centrifugation, which tends to compact the nanocluster pellet to such a extent as to render redissolution in non-polar solvents almost impossible. All of these problems are avoided by the extraction method.

Solid phase extraction. Solid-phase extraction cartridges are available (e.g. Water's corp. Sep-Pak) containing the same types of materials used in HPLC columns. These disposable cartridges of organically functionalized silica, alumina or ion exchangers are able to retain polar or ionic materials while passing non-polar ones like alkane thiol stabilized Au nanoclusters. They are commonly used to concentrate analytes by large amounts prior to chemical analysis, but we have found they also work well for purifying nanoclusters. The final nanocluster solution purity after two to three passages through the cartridge is quite good, as demonstrated by HPLC analysis of the cluster solution.

Surface passivation. Alkyl thiols of various chain lengths, **Table IV**, were dissolved in decane to a 0.5 M concentration. These alkyl thiols were added to the nanocluster solutions to give a final concentration of 0.01 M. In general, we found that the thiols with alkane chains of 6 carbons or shorter resulted in the immediate precipitation of the nanoclusters, causing, for example, a wine red Au nanocluster solution to form a blue precipitate. (The color change upon precipitation is a complex issue that is really only partially understood in terms of the Mie scattering from vicinal particles.) Likewise, samples capped with the longer chain thiols ($C_{16}SH$, $C_{18}SH$) precipitated, but not as quickly. Thus the ability to control the particle gaps in superlattices is limited by the observed stability window.

Lability. Attempts to cap Au nanoclusters with the shorter chain thiols (C_3SH – C_6SH) results in precipitation, providing an avenue for ascertaining the lability of the capping agents. Several experiments were conducted in this regard. Adding hexanethiol (C_6SH) to a solution previously capped with dodecanethiol ($C_{12}SH$) appeared to have no visual effect on the color and stability of the solution, possibly indicating the irreversible binding of $C_{12}SH$ to the Au nanoclusters. In contrast, adding C_6SH to solutions to which BUSH, $C_{16}SH$, or $C_{18}SH$ had been added causes the nanoclusters to precipitate, indicating that these particular thiols either do not stick to the Au cluster surfaces at all, or are very labile. It seems reasonable that thiols having long alkane chains are more soluble in the hydrophobic solvents, so that there is little preferential adsorption onto the cluster surface.

We also conducted some inverse experiments. $C_{12}SH$ was added to an **Au 621** sample that had been precipitated with C_6SH. The dark blue precipitate went back into solution, forming a beautiful wine red sol, indicating hexanethiol is very labile. This technique of precipitate resuspension worked for precipitates as old as 55 days. TEM images of these clusters demonstrate the existence of very regular 2-D superlattices.

Results

Superlattice formation. The successful formation of superlattices from unfractionated nanoclusters depends on the right combination of oil, surfactant, reducing agent, metal salt, stoichiometry, surface passivator, elapsed time before passivating, and sample aging time. Some of the salient aspects of these issues are briefly addressed in the following.

Substrate and solvent effects. Before discussing the detailed reaction conditions under which nanoclusters that form superlattices are made, it is first helpful to describe the manner in which superlattice crystals can be grown. To form crystals, an aliquot of the solution was deposited on a substrate and allowed to evaporate at a slow rate. Slow evaporation could be accomplished by adding a nonvolatile solvent, such as dodecane, at 25 vol. %, and/or by covering the solutions with a Petri dish.

A variety of substrates utilized for 3-d crystal growth, including graphite, paraffin, Mylar™, Teflon™, natural mica, glass, silicon, and lanthanum aluminum oxide.

Graphite was too porous, and paraffin was not compatible with the oil the clusters were suspended in. For the substrates with hydrophilic surfaces, the applied droplet had to be contained within a ring of inert grease (e.g. Krytox™) to prevent spread of the droplet. Although our first 3-d crystals were successfully grown on a glass substrate, other substrates proved to work better. In particular, we found that Teflon™ was very effective, since it has a low surface tension that allows the droplets to be contained by surface tension, which results in a low surface area for solvent evaporation, thus encouraging the formation of large crystals.

On Teflon™, large areas of concentrated nanoclusters formed and faceted crystals nucleated from the edges, as shown in the images of **Au 421**, discussed below. Higher alkanes added to the solutions at 25 vol.% slowed evaporation and improved crystal growth in those samples prepared in the more volatile oils.

Crystals. Making superlattices from Au nanoclusters synthesized in inverse micelles proved easy, due to the tendency of Au nanoclusters to form spherical, monodisperse particles. The first 3-D Au crystals, **Fig. 2**, were grown from **Au 421** nanoclusters, prepared by dissolving hydrogen tetrachloroaurate(III) in a 10 wt% $C_{12}E_4$/decane inverse micelle solution. This precursor solution was then reduced with 0.2 M $LiAlH_4$/THF and capped the following day with dodecanethiol. Following NMF extraction 2 μl of the Au solution was deposited on a Teflon™ substrate and allowed to dry at room temperature. This sample also forms the 2-D arrays in **Fig. 2**.

The tendency to crystallize is sufficiently strong that it is even possible to grow superlattice crystals from a solution of alkane thiol capped nanoclusters that had not had the surfactant extracted, as shown in **Fig. 3** for **Au 427**. The same is true of the 2-d arrays on TEM grids, although the image quality is greatly reduced by the presence of the surfactant.

Good crystals were formed from **Au 461**, which was prepared in pentane and aged at room temperature for 87 days. 25% dodecane was then added to this solution, and an aliquot was deposited on a glass slide, producing the nearly perfect hexagonally shaped crystals shown in **Fig. 4**. The conditions that determine the crystal morphology are not really understood at this point.

Many other Au samples were made that formed superlattice crystals. The best combination of reaction conditions we found is $C_{12}E_5$ for the surfactant, decane for the oil, and Super Hydride for the reducing agent, in a 4:1 molar ratio. Capping with the selected range of thiols is then done 1 hour after reduction, since Au nanocluster solutions blacken and sediment if thiol capping is done too soon after reduction. It is on samples prepared in this manner (e.g. **Au 621**) that the effect of the alkane thiol chain length on interparticle spacing was determined. Nanocluster size is important in whether or not a particular sample will form superlattices; we did not have much success with very small clusters, at least in the formation of 3-D superlattices.

Image analysis. Nanoclusters that form superlattices are different from molecules that form crystals in that a significant size distribution occurs. A large size distribution can prevent the formation of large coherent domains and in extreme cases even prevent crystallization. To obtain information such as the coherent domain size from molecular crystals, one uses x-ray or neutron diffraction, where such properties are computed from the linewidth. The interpretation of the linewidth of the superlattice reflections is not as clear, since it is affected by both crystalline domain size and cluster polydispersity. An example of this is given in **Fig. 5**, where the crystalline domain size is quite large, but the translational symmetry of the superlattice is compromised by polydispersity, with the small clusters tending to crystallize at the edge of the domain, an effect first reported and understood by Heath and co-workers[12].

Fortunately, nanoclusters are sufficiently large that real space data in the form of TEM images are easily obtained, and these contain information that is directly accessible. To this end we have developed software that enables the accurate determination of many of the parameters associated with 2-D superlattices. In the following is a description of the information that can be obtained, as well as a brief description of the algorithms.

Cluster positions. The first step in image analysis we call FindClusters. The primary goal of this program is to accurately determine the size, shape, and center of mass position of all the acceptable nanoclusters in a TEM image. Distribution functions of cluster mass, radius, etc. can then be computed, as well as moments of these

distributions. The radial pair correlation function of the particle centers of mass are also computed, and a file of particle coordinates is created for further analysis.

In the first stage of this program we attempt to make clear distinction between the nanoclusters and the TEM holey carbon grid. On good images this process is simple, and for clarity we use as an example the relatively good image in **Fig. 6**, which is **Au646** coated with C_8SH, though this process works well even with extremely poor images. The example image is first processed so that the grayscale values of the pixels indicating particles exceed those of all of the pixels indicating the grid. The image can then be thresholded to a binary image wherein all of the particle pixels have the maximum grayscale value of 255, and the grid pixels have a grayscale value of 0. We approach this problem by two methods, convolution and conditional thresholding.

Convolution -- In the first approach the image is convoluted with an operator that is roughly the second derivative of a Gaussian. The integral of this 2-D function is zero in the plane, so when applied to a uniform region of the image, a zero result is obtained. The convolution is done point-wise, with global update, and when the radius of the convolution operator is appropriately chosen so that the positive part of the function just covers the particles, the resulting processed image shows readily discernable boundaries around diffuse particles, and is readily thresholded, **Fig. 7**. The convolution approach is only useful for determining the particle centers, since particle size information is obliterated by the operator, and is most effective when the polydispersity is not too large.

Conditional thresholding -- When particle size information is required, a different approach is taken. First, the image is moderately smoothed, by replacing each pixel value by an unweighted average of itself and the average of its neighbors. Then a conditional thresholding technique is applied, whereby a pixel is set to 255 if its value exceeds a selected threshold value *and* 40% of its 8 nearest neighbors exceed that value. This insures that noise from the grid does not appear as small particles. The result of these operations is the effectively thresholded image in **Fig. 8**.

Particle size determination. The next task is the efficient enumeration and quantification of the particles. To accomplish this, each pixel is assigned a unique identifying number. The image array is then repeatedly scanned, and each pair of neighboring pixels that are assigned the grayscale value 255 have their pixel IDs changed

to that of the lower ID of the pair. The image is scanned until no further ID changes occur. The result of this is that every connected cluster of black pixels consists of pixels with the same ID. No two disconnected clusters will have the same ID. It is now simple to compute the areas of all the clusters, and their projected radii of gyration - the root mean square separation of the pixels from their center of mass. Also, the ratio of their area to their radius of gyration is computed, which is a maximum for round clusters.

Particle discrimination. The next stage of processing is discrimination. Not every resolved feature should be counted as a cluster. For example, overlapping particles should be excluded, as well as those particles that contact a border of the image. In some cases it may be desirable to delete features of the image that are too small, too large, or unusual in shape. These criteria can be selected by setting various discrimination gates. For example, in the image in **Fig. 8** the discriminated particles are shown in gray, and the final included particles are shown in black.

The accepted particles are now analyzed. Once again, their area and radius is determined, and the size distribution is computed. Also, their radial pair correlation function is computed, and a binary file of particle coordinates is written, to be read by a rendering program we call Balls, and by the analysis program HexDomains. A rendering of the final particle coordinates is given in **Fig. 9.**

Hexagonal domains. The hexagonally packed domains are now enumerated and quantified using a program called HexDomains, which determines a wide variety of structural parameters from the array of particle coordinates. The first step is the determination of the neighbors of each of the particles. Neighbors determination is an N^2 problem when approached in a straightforward way, but we have developed a fast, linear-N algorithm that for N=10,000 particles accomplishes this task in much less than a second on a typical desktop computer.

The next step in the analysis is the determination of the type of location in which a particle resides. There are many possible categories, principal of which are hexagonal sites, hexagonal edge sites, hexagonal defect sites at the boundaries of hexagonal domains of different orientation, and stacked hexagonal sites, a category that applies only to those cases where 3-D information is available, such as in simulations of crystal

formation. The site type determination is based on complex criteria, including the number of neighbors, "bond" angles, etc.

The crystalline domains are then determined by a type of multidimensional percolation. In the normal percolation problem neighbors are defined by physical proximity alone. It is possible to include other criteria to determine bonding, and we stipulate the particle orientations also agree within a small acceptable amount, typically about 3°. The particle orientation is defined for hexagonal particles by the angle, between -30° and +30°, needed to rotate the crystal in which the particle resides so that contacting chains of hexagonal spheres align with the y (vertical) axis. The result of this percolation process is the enumeration of all the crystalline domains in the array, **Fig. 9**.

Lattice spacing. Once the crystalline domains are determined it is possible to accurately compute the lattice spacing of the array. One simple approach to this problem, that works well only for high quality arrays, is to compute the radial or vector pair correlation function of the particle centers of mass alone. This is an improvement on a diffraction experiment, because the diffraction pattern is convoluted with the particle form factor (a Bessel function for a sphere), but with image processing it is possible to do better still, by excluding particles that are not in hexagonal sites, such as those at domain boundaries etc., and by excluding interdomain correlations.

The *intradomain* correlation function is computed by orienting each domain so that chains of hexagonal particles lie along the y (i.e. vertical) axis. This results in the vector pair correlation function of **Fig. 10**. It is possible to obtain accurate values of the lattice spacing from these data. For disordered lattices substantially more disordered than the example given here, the intradomain function can be substantially better than the total function, which might only appear as a few diffuse rings with poor signal to noise, due to the large incoherent background caused by the disordered regions. The particle gaps, determined by the choice of capping agent, can be determined by subtracting the average particle diameter from the lattice spacing.

Control of interparticle gaps. To explore the control of interparticle spacing on thiol chain length we divided a freshly synthesized Au nanocluster solution into a number of aliquots, and added to each of these thiols from C_6SH to $C_{18}SH$ in steps of even carbon

numbers. At this point, the solution with C_6SH immediately formed a dark blue precipitate, the solutions capped with C_8SH, $C_{10}SH$, $C_{12}SH$, and $C_{14}SH$ remained wine red (and are indefinitely stable), and the solutions capped with $C_{16}SH$ and $C_{18}SH$ changed color slowly, eventually forming a blue precipitate.

These solutions were immediately deposited on holey carbon grids, and TEM images of the resultant arrays were collected in a single day, to minimize aging effects. Some aspects of these images are immediately apparent; samples capped with C_6SH show the formation of small 3-d superlattices, but 2-d layers are not found, indicating that the formation of crystalline domains occurs very quickly in solution, resulting in the aforementioned color changes. Nanoclusters capped with C_8SH to $C_{14}SH$ show ordered 2-d lattices, indicating that the clusters remain fully dispersed in solution until the solvent evaporates on the grid. Nanoclusters capped with $C_{16}SH$ and $C_{18}SH$ show a wide size distribution and do not form ordered arrays.

Using the software described above, the size distributions of the capped nanocluster solutions were determined, with selected results in **Fig. 11**. There is a definite trend to a much broader size distribution as the alkane chain length increases. We believe this is due to the fact that as the chain length increases the thiol becomes more soluble in the hydrophobic oil decane. Thus a ligand can coordinate with a gold atom, dissolve in solution, and redeposit this on another cluster, causing a marked increase in polydispersity, until in the case of $C_{16}SH$ and $C_{18}SH$ ordered arrays no longer form.

We used the image analysis software to resolve the hexagonal domains and compute the intradomain vector pair correlation functions for the range of samples. From these data, and similar data for the other samples, we are able to determine the lattice spacing. The one exception was **Au 646** capped with C_6SH, for which the particles did not form 2-d arrays, but did form 3-d arrays. For this sample we did the analysis essentially by hand, using only the elementary tools available in the application NIH Image. In essence, we looked for ordered regions within the 3-d crystals, and measured the interparticle separation in many locations, usually over regions of at least 5 particles in linear extent, to minimize errors associated with estimating the particle centers.

The dependence of the average nanocluster size on the thiol chain length is shown in **Fig. 12.** Data for the $C_{16}SH$ and $C_{18}SH$ samples are not included, since they did not form ordered hexagonal arrays. The dependence of the cluster size is nonmonotonic, reaching a maximum at the $C_{10}SH$ sample. By subtracting this from the measured lattice spacing, the particle gaps are obtained, as shown in **Fig. 12.** Fitting these data gives an increase in the particle gap of 1.2Å per carbon atom, which is roughly half that expected from HPLC studies of the capped nanoclusters in solution. The thiol chains either collapse somewhat upon solvent evaporation, or tend to interdigitate.

Effect of gaps on dielectric properties

Now that we have demonstrated the synthesis of superlattices of controlled particle size and lattice spacing, it is interesting to investigate the properties of these materials. The dielectric constant of the superlattice is interesting, because it depends on achieving high particle loadings, which is not easily achieved with randomly dispersed particles, and is sensitively dependent on the thickness of the capping layer and the lattice geometry. Consideration of the dielectric constant also leads to some implications for the use of these materials in supercapacitors.

Dipole moment of a nanoparticle in an applied field. It is helpful to first consider the polarization of a particle in a vacuum. When a particle is placed in an initially uniform field $\mathbf{E}_0$, the particle polarizes, producing an induced field that opposes the initially uniform field. This induced field is dipolar outside the particle, but inside the particle the field is constant for solid ellipsoidal shapes, and generally complex for nonellipsoidal shapes. In any case, when the particle dielectric constant is greater than that of the surrounding medium, the induced field inside the particle opposes the applied field, so that the internal field is far less than one might expect. In fact, one might expect that the dipole moment $\mathbf{m}$ of a nanoparticle would be given by $\mathbf{m} = \frac{4\pi}{3} a^3 \chi \mathbf{E}_0$, where a is the particle radius and χ is the susceptibility of the material of which the particle is made, but this expression does not account for the self-interaction, and so is manifestly incorrect.

It has been found that the internal field of a solid ellipsoidal dielectric can be expressed as [1]

$$\mathbf{E}_{in} = \mathbf{E}_0 - n\frac{\mathbf{P}}{\varepsilon_0} \tag{1}$$

where n is the so-called depolarization factor of the particle, which is a function of the particle aspect ratio, but not of the susceptibility of the material of which the particle is composed, and is between 0 and 1. For nonellipsoidal shapes the situation is more complex, because the internal field is nonuniform. Then one must talk in terms of the average internal field, $\overline{\mathbf{E}}_{in} = \mathbf{E}_0 - n\frac{\overline{\mathbf{P}}}{\varepsilon_0}$ and the depolarization factor n is now a function of the material susceptibility, and is only practically computed via finite difference or finite element methods.

Returning to the ellipsoidal particle case, the polarization inside the particle can be written in terms of the internal field $\mathbf{P} = \chi\mathbf{E}_{in}$. Substituting this into Eq. 1 then gives an expression for the internal field, $\mathbf{E}_{in} = \frac{\mathbf{E}_0}{1+n\chi/\varepsilon_0}$. The particle polarization can then be expressed in terms of the applied field, $\mathbf{P} = \frac{\chi}{1+n\chi/\varepsilon_0}\mathbf{E}_0$ and the *particle susceptibility* is then

$$\chi_p = \frac{\chi}{1+n\chi/\varepsilon_0}. \tag{2}$$

It should be noted that for metal nanoclusters one expects the material susceptibility to be essentially infinite, so that $\chi_p = \frac{\varepsilon_0}{n}$. Note that in this limit the material susceptibility is unimportant, and the particle susceptibility is a function of particle shape alone.

For prolate ellipsoidal particles the depolarization factor parallel to the long axis of the particle is [2]

$$n_{\|} = \frac{1}{g^2-1}\left[\frac{g}{2\sqrt{g^2-1}}\ln\left(\frac{g+\sqrt{g^2-1}}{g-\sqrt{g^2-1}}\right)-1\right] \tag{3}$$

where $g=b/a$ is the particle aspect ratio in terms of the long axis b and the short axis a. The perpendicular depolarization factor is just $(1-n_{\|})/2$, so that the sum of the three principal depolarization factors is 1. For the special case of spherical particles, the depolarization factor is thus 1/3, and the particle susceptibility can be written $\chi_p = 3\varepsilon_0 \frac{\kappa-1}{\kappa+2} = 3\varepsilon_0\beta$ where the material dielectric constant is $\kappa - 1 = \chi/\varepsilon_0$. The dipole moment of the particle can now be expressed as $\mathbf{m} = \frac{4\pi a^3}{3}\mathbf{P} = \frac{4\pi a^3}{3}\chi_p \mathbf{E}_0 = 4\pi a^3 \varepsilon_0 \beta \mathbf{E}_0$. In the more general case of a particle in a dielectric continuum of dielectric constant κ_c the particle susceptibility is

$$\chi_p = 3\varepsilon_0\kappa_c \frac{\kappa-\kappa_c}{\kappa+2\kappa_c} = 3\varepsilon_0\kappa_c\beta \qquad (4)$$

and the dipole moment is $\mathbf{m} = 4\pi a^3 \varepsilon_0 \kappa_c \beta \mathbf{E}_0$.

Effective dielectric constant. We have considered thus far the polarization of an isolated nanoparticle. In nanoparticle assemblies the situation is more complex, since the field at the particle is not merely the applied field, but contains contributions from all of the dipoles in the system, as well as multipolar fields from the nearby particles. Fortunately, these multipolar fields decay rapidly, and can be ignored for capped nanoparticles to a good approximation, due to the large relative particle spacing. The dipolar fields cannot be ignored, and to compute the effective dielectric constant of the particle assemblies we must first compute the local field, which we do using the method of Lorentz. In the following we assume the particles are in a vacuum, and correct the final result for the dielectric constant of the surrounding medium.

The local field $\mathbf{E}_{loc} = \mathbf{E}_0 + \mathbf{E}_{LC} + \mathbf{E}_{dip}$ can be thought of as the sum of three contributions [1], the applied field $\mathbf{E}_0$, the Lorentz cavity field $\mathbf{E}_{LC}$, and the field due to the local dipoles, $\mathbf{E}_{dip}$. The Lorentz cavity field is due to the bound surface charge density on the surface of an imaginary cavity centered on the dipole of interest. This surface charge density is just the surface normal to the polarization density of the material. Integrating over the surface of a spherical cavity gives

$$\mathbf{E}_{LC} = \frac{\mathbf{m}}{3\varepsilon_0 v} \tag{5}$$

where the volume per dipole is $v = \frac{4\pi a^3}{3\phi}$. Note that this result is independent of the cavity size, which we take to be larger than any structural correlation length of the nanoparticle assemblies.

The field due to the nearby dipoles, i.e. those within the spherical cavity, is

$$\mathbf{E}_{dip} = -\frac{\mathbf{m}}{2\pi\varepsilon_0 a^3}\psi_2 \quad \text{where} \quad \psi_2 = -\sum_{j\neq i}\left(\frac{a}{r_{ij}}\right)^3 \frac{3\cos^2\theta_{ij} - 1}{2} \tag{6}$$

Here θ is the angle that the line of centers between two particles makes to the applied field direction. Substituting the result $\mathbf{m} = 4\pi a^3 \varepsilon_0 \beta \mathbf{E}_{loc}$ for the particle dipole moment in a vacuum into Eqs. 5&6, the local field can be found,

$$\mathbf{E}_{loc} = \frac{\mathbf{E}_0}{1 - \beta(\phi - 2\psi_2)} \tag{7}$$

For large volume fractions of particles, the local field can be several times the applied field. The dielectric constant is given by the dipole moment density

$$\mathbf{P} = \varepsilon_0(\kappa_{eff} - 1)\mathbf{E}_0 = \frac{\mathbf{m}}{v} = 3\varepsilon_0\beta\phi\mathbf{E}_{loc} \tag{8}$$

with the result

$$\kappa_{eff} = \kappa_c \frac{1 + 2\beta(\phi + \psi_2)}{1 - \beta(\phi - 2\psi_2)} \tag{9}$$

where we have included the effect of the dielectric constant of the surrounding medium. Note that presence of metal nanoparticles in a dielectric medium is to enhance the dielectric constant by the same fraction, regardless of the dielectric constant of the medium, so long as it is much smaller than that of the dielectric.

Numerical results. The expected dielectric constants for various lattices of *uncapped* nanoparticles were computed, with the results in **Table V**. Note that for the cubic lattices the dipolar sum is identically zero by symmetry. For the fcc and hcp lattices the field direction is assumed orthogonal to the stacked hexagonal planes, which is relevant to experiments on crystals grown on flat substrates. Note that the results for the hcp and fcc lattices are very similar, which indicates that these results should apply even to randomly stacked planes.

The results for the body centered tetragonal (bct) lattice are with the particle chains aligned along the applied field, and this state actually minimizes the electrostatic free energy of the system, and thus maximizes the dielectric constant enhancement to a value of nearly 10. This lattice is in fact the ground state for polarized hard spheres. It is possible that crystallization of nanoparticles in a large applied field could achieve this lattice, despite the slightly lower packing density.

For capped nanoclusters the effective dielectric constant can be written as

$$\kappa_{eff} = \kappa_c \frac{1+2\alpha^3\beta(\phi+\psi_2)}{1-\alpha^3\beta(\phi-2\psi_2)} \qquad (10)$$

where α is the ratio of the metal particle diameter to the particle spacing in the lattice. This function is plotted for the fcc lattice in **Fig. 13**. For a typical value of a = 3/4 achieved with alkane thiol capping agents, the dielectric enhancement factor of ~2.4 is actually considerably smaller than its maximum value of 9.56, and the self-consistent point dipole computation actually underestimates the effective dielectric constant at small particle spacings. Increased particle sizes could increase this ratio, as could the discovery of much smaller effective capping agents.

Application to supercapacitors. If the effective dielectric constant of metal nanocluster superlattices could be increased, these materials might have applications as

dielectrics for supercapacitors. The idea of using particle composites for such applications is not new, and is generally discredited because experimental measurements on mesoscale particles have conclusively shown that the higher dielectric constant of the material is more than offset by a decrease in the dielectric breakdown field. There are essentially three factors that reduce dielectric standoff. First, mesoscale particles are invariably rough on some supra-atomic scale, causing classical edge singularities in the electric field near surface asperities. These large field enhancements can initiate an electron avalanche. Second, large particle suspensions will have gaps between vicinal particles that are small compared to the particle diameters. To first order, the field enhancement in the gap will be the ratio of the particle diameter to the gap (in the limit of infinite particle dielectric constant) so large field enhancements will occur, leading to breakdown initiation. Third, the large size of the gaps in mesoscale particle systems can easily allow for an electron avalanche to occur before an electron runs into a second particle. Nanoclusters address each of these problems, because surface asperities are at the atomic level, particle gaps are a controlled and significant fraction of the particle diameter, and the gap size is small enough that electron avalanches might be stopped by collisions with nanoclusters. Thus we believe that these materials might be a possible candidate for high energy density supercapacitors that also have high power densities.

Conclusions

We have shown that it is possible to control the interparticle spacing of superlattices over a limited range by capping with organic thiols. Very small alkanethiols cause precipitation, and high alkanethiols restructure the nanoclusters, but intermediate alkane thiols, from C_6SH to $C_{14}SH$, result in the formation of uniform superlattices with controlled interparticle spacings. Using image analysis of TEM images of nanocluster arrays we conclude that the polydispersity of the nanoclusters increases with the alkanethiol chain length, presumably due to thiol-mediated coarsening, which is assisted by the increased solubility of the long-chain thiols in high alkanes. From image analysis techniques we can also accurately compute the intradomain vector pair correlation

function from TEM images, and find that the particle gaps increase at the rate of 1.4 Å per carbon atom of the alkane thiols.

The control of the particle spacings is important to some potential applications, such as the effective dielectric constant and dielectric breakdown strength of nanocomposites. It is argued that these materials might have applications to supercapacitors, and future research will address this issue.

References

1. Boutonnet, A.; Kizling, J.; Stenius, P.; Maire G. *Colloids and Surfaces*, **1982**, *5*, 209-225.
2. Wilcoxon, J. P.; Williamson, R. L. Proceedings of the Fall Materials Research Society, Boston, MA **1989**.
3. Wilcoxon, J. P.; Williamson, R. L. *J. Chem. Phys.* **1993**, *98*, 9933-9950.
4. Wilcoxon, J. P.; Provencio, P. P. *J. Phys. Chem. B* **1999**, *103*, 9809-9812.
5. Giersig, M.; Mulvaney, P. *J. Phys. Chem.* **1993**, *97*, 6334-6336.
6. Enustun, B. V.; Turkevich, J. *J. Amer. Chem. Soc.* **1963**, *85*, 3317.
7. Brust, M.; Walker, M.; Berthell D.; Schiffrin D. J.; Whyman, R. *J. Chem. Soc., Chem Comm.* **1994**, 801-802.
8. Brust, M.; Berthell D.; Schiffrin D. J.; Kiely, C. J. *Adv. Mater.*. **1995**, *7*, 795-797.
9. Leff, D. V.; Ohara, P. C.; Heath, J. R.; Gelbart, W. M. *J. Chem. Phys.* **1995**, *99*, 7036-7041.
10. Alvarez, S. M.; Khoury, J. T.; Shaaff, T. G.; Shafigullin M. N.; Vezmar, I.; Whetten, R. L. *J. Chem. Phys.* **1997**, *101*, 3706-3712.
11. Whetten, R. L.; Khoury, J. T.; Alvarez, S. M.; Murthy, S.; Vezmar, I.; Wang, Z. L.; Stephens P. W.; Cleveland, C. L.; Luedtke, W. D.; Landman, U. *Adv. Mater.*. **1996**, *8*, 428-433.
12. Ohara, P. C.; Leff, D. V.; Heath, J. R.; Gelbart, W. M. *Phys. Rev. Lett.* **1995**, *75*, 3466-3469.
13. Andres, R. P.; Bielefeld, J. D.; Henderson, J. I.; Janes, D. B.; Kolagunta, V. R.; Kubiak, C. P.; Mahoney, W. J.; Osifchin, R. G. *Science* **1996**, *273*, 1690-1693.

14. Sarathy, K. V.; Raina, G.; Yadav, R. T.; Kulkarni, G. U.; Rao, C. N. R.; *J. Phys. Chem. B* **1997**, *101*, 9876-9880.
15. Korgel, B. A.; Fullam, S.; Connolly, S.; Fitzmaurice, D. *J. Phys. Chem.* **1998**, *102*, 6579-6588.
16. Taleb, A.; Petit, C.; Pileni, M. P. *J. Chem. Phys. B* **1998**, *102*, 2214-2220.
17. Fink, J.; Kiely, J.; Bethell, D.; Schiffrin, D. J. Chem. Mater. **1998**, *10*, 922-926.
18. We were not able to repeat this synthesis with R groups larger than C_{12}, due to the fact that these surfactants do not make inverse micelles in toluene, even in the presence of the·Au salt. In fact, for R groups larger than C_8, these surfactants do not form micelles without the Au salt. It is possible a cosurfactant had been added to their solutions, however addition of typical cosurfactants such as hexanol does not lead to micelle formation.

Table I

Solution compositions for selected Au nanoclusters

Sample	Salt	Surfactant	Oil	Reducing Agent	R	Thiol
Au 421	$HAuCl_4$-$4H_2O$	$C_{12}E_4$	C10	0.2 M $LiAlH_4$/THF	5.33	$C_{12}SH$, next day
Au 427	$HAuCl_4$-$4H_2O$	$C_{12}E_5$	C10	1.0 M Super-Hydride®	1.33	$C_{12}SH$, 7 hrs
Au 461	$HAuCl_4$-$3H_2O$	$C_{12}E_5$	C5	1.0 M Super-Hydride®	1.33	$C_{12}SH$, 3 hrs
Au 494	$HAuCl_4$-$3H_2O$	$C_{12}E_5$	C16	0.2 M $LiAlH_4$ bis-THF	5.33	aged, $C_{12}SH$
Au 513	NH_4AuCl_4-XH_2O	$C_{12}E_6$	C10	0.2 M $LiAlH_4$/toluene	5.33	aged, $C_6 \rightarrow C_{18}SH$
Au 621	NH_4AuCl_4-XH_2O	$C_{12}E_5$	C12	1.0 M Super-Hydride®	1.33	$C_6 \rightarrow C_{18}SH$, 1 d
Au 646	NH_4AuCl_4-XH_2O	$C_{12}E_5$	C16	1.0 M Super-Hydride®	1.33	$C_6 \rightarrow C_{18}SH$, 1 d

Table II

Partitioning ratios of the nonionic surfactant $C_{12}E_4$ in selected solvents

Surfactant	Oil	Solvent	Partitioning Ratio
$C_{12}E_4$	decane	ethylene glycol	1.50
$C_{12}E_4$	decane	water	0.00
$C_{12}E_4$	decane	dimethylformamide	17.00
$C_{12}E_4$	decane	formamide	1.76
$C_{12}E_4$	decane	n-methylformamide	37.00
$C_{12}E_4$	decane	methanol	0.78

Table III

Measured surfactant partitioning coefficients

Surfactant	Oil	Solvent	Partitioning Ratio
$C_{12}E_3$	decane	n-methylformamide	2.55
$C_{12}E_4$	decane	n-methylformamide	37.00
$C_{12}E_5$	decane	n-methylformamide	118.00
$C_{12}E_6$	decane	n-methylformamide	90.00
$C_{12}E_7$	decane	n-methylformamide	99.00
$C_{12}E_8$	decane	n-methylformamide	∞

Table IV

Hydrophobic capping ligands

Capping Ligand	AKA
1-propanethiol	1-C_3SH
2-propanethiol	2-C_3SH
t-butanethiol	BUSH
1-butanethiol	C_4SH
pentanethiol	C_5SH
hexanethiol	C_6SH
octanethiol	C_8SH
decanethiol	$C_{10}SH$
dodecanethiol	$C_{12}SH$
tetradecanethiol	$C_{14}SH$
hexadecanethiol	$C_{16}SH$
octadecanethiol	$C_{18}SH$

Table V

Dielectric constants for various lattices

lattice	ϕ	Ψ_2	κ_{eff}/κ_c
sc	0.523	0	4.30
fcc	0.740	0	9.56
hcp	0.740	-0.0004	9.59
bct	0.698	-0.032	9.82

Figure Captions

Fig. 1. TEMs of **Au 513**, (left) sample was thermally annealed at 70°C for 15 hours and (right) sample was left uncapped at ambient for 32 days, cluster size increased with time.

Fig. 2. **Au 421** superlattices. TEM of 2-d superlattices of **Au 421**, magnification 50 kx (top). Optical image of **Au 421** crystals starting to form from edges of nanocluster rich areas, 25% nonvolatile dodecane was added to reduce the rate of solvent evaporation and thus crystal growth (250x magnification.)

Fig. 3. Optical image of **Au 427** as synthesized, no extraction of surfactant, 250x.

Fig. 4. **Au 461** hexagonal crystal grown from solution 87 days after synthesis & surfactant extraction, 2500x.

Fig. 5. Example of an Au array showing size fractionation effects.

Fig. 6. A reasonably clear test image with only a few problems, including a slight over focus causing an apparent light center at each particle, some clustering and contacting particles. This image is of **Au 646** nanoclusters coated with C_8SH.

Fig. 7a. The result of the test image convoluted with the hat operator. Particle size information is not retained, but the particle centers of mass can be accurately determined.

Fig. 7b. The convoluted test image is thresholded, and discriminated. Discrimination removes undesirable particles, such as those contacting the image borders and those having aspherical shapes. The gray shaded particles are those that are removed.

Fig. 8. The smoothed and conditionally thresholded image after discrimination. The gray particles were removed because they contact an image border or other particles. Size discrimination was not used to create this image.

Fig. 9. The hexagonal domains in this sample are resolved and shown in a pseudoball representation. Particles are given a grayscale value unique to their domain.

Fig. 10. The intradomain vector pair correlation function allows the lattice spacing to be extracted with high precision.

Fig. 11. The size distribution of selected capped Au nanoclusters shows a definite trend to larger nanoclusters and a broader size distribution as the alkane thiol chain length increases.

Fig. 12a Dependence of the average cluster size and lattice spacing on thiol chain length.

Fig. 12b Dependence of the nanocluster gap on thiol chain length.

Fig. 13. The dielectric enhancement of the fcc lattice is shown as a function of the ratio of the core diameter to the particle spacing.

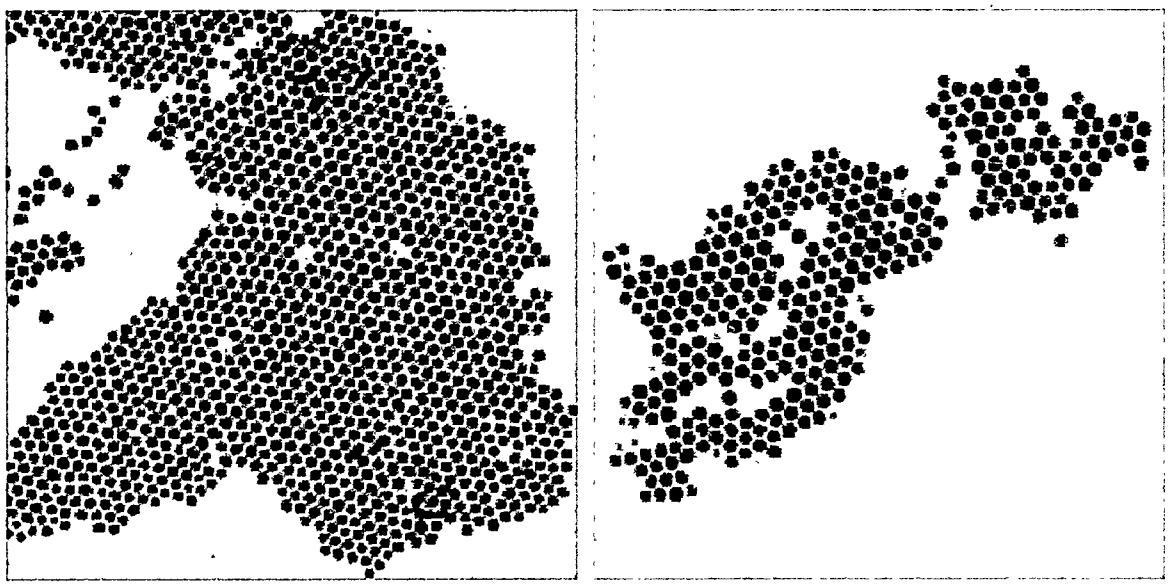

Figure 1 Martin et al

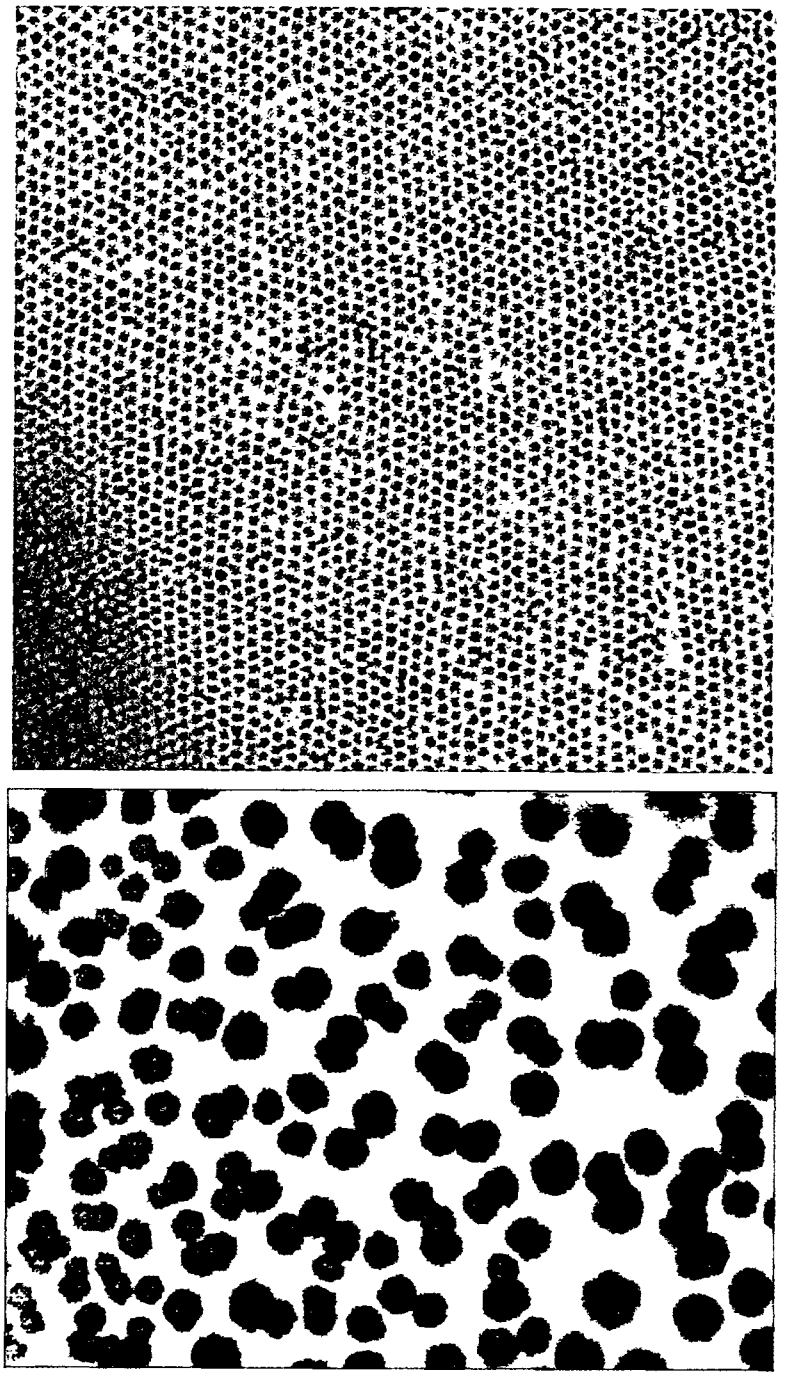

Figure 2 Martin et al

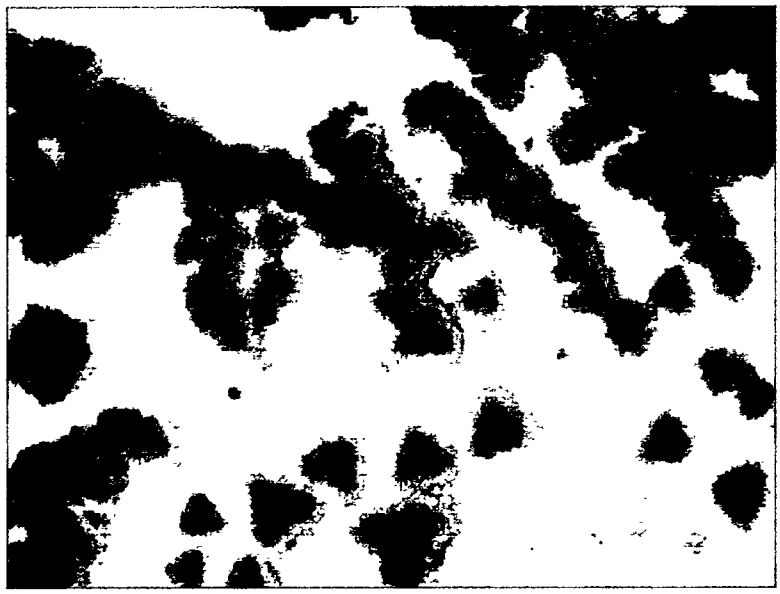

Figure 3 Martin et al

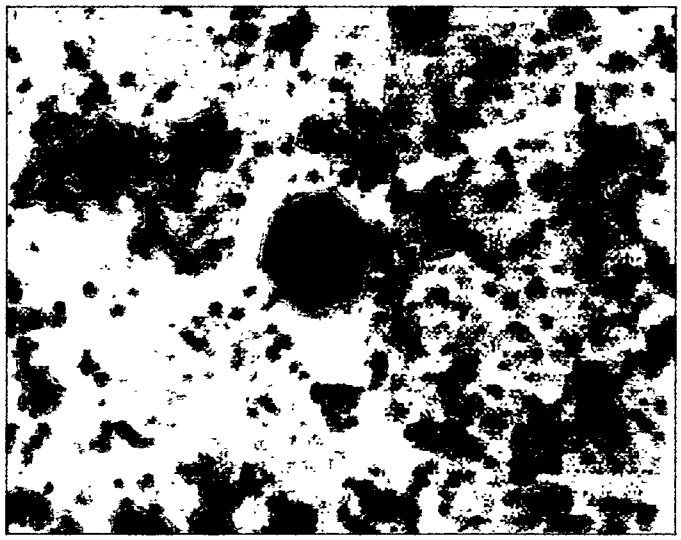

Figure 4 Martin et al

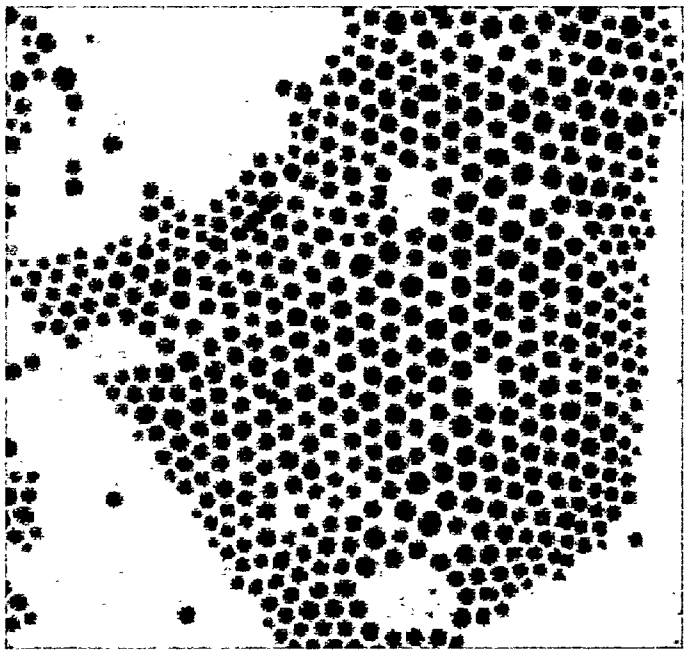

Figure 5 Martin et al

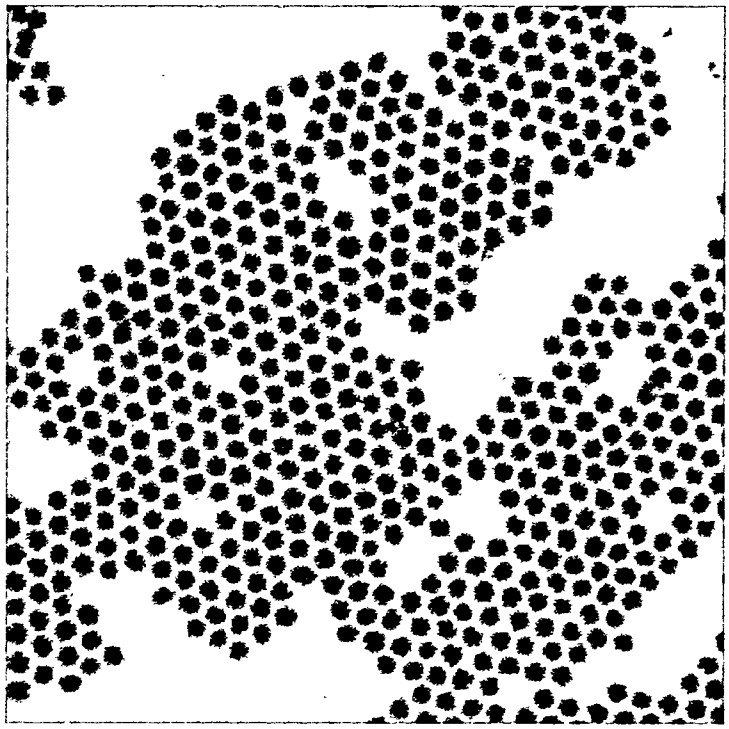

Figure 6 Martin et al

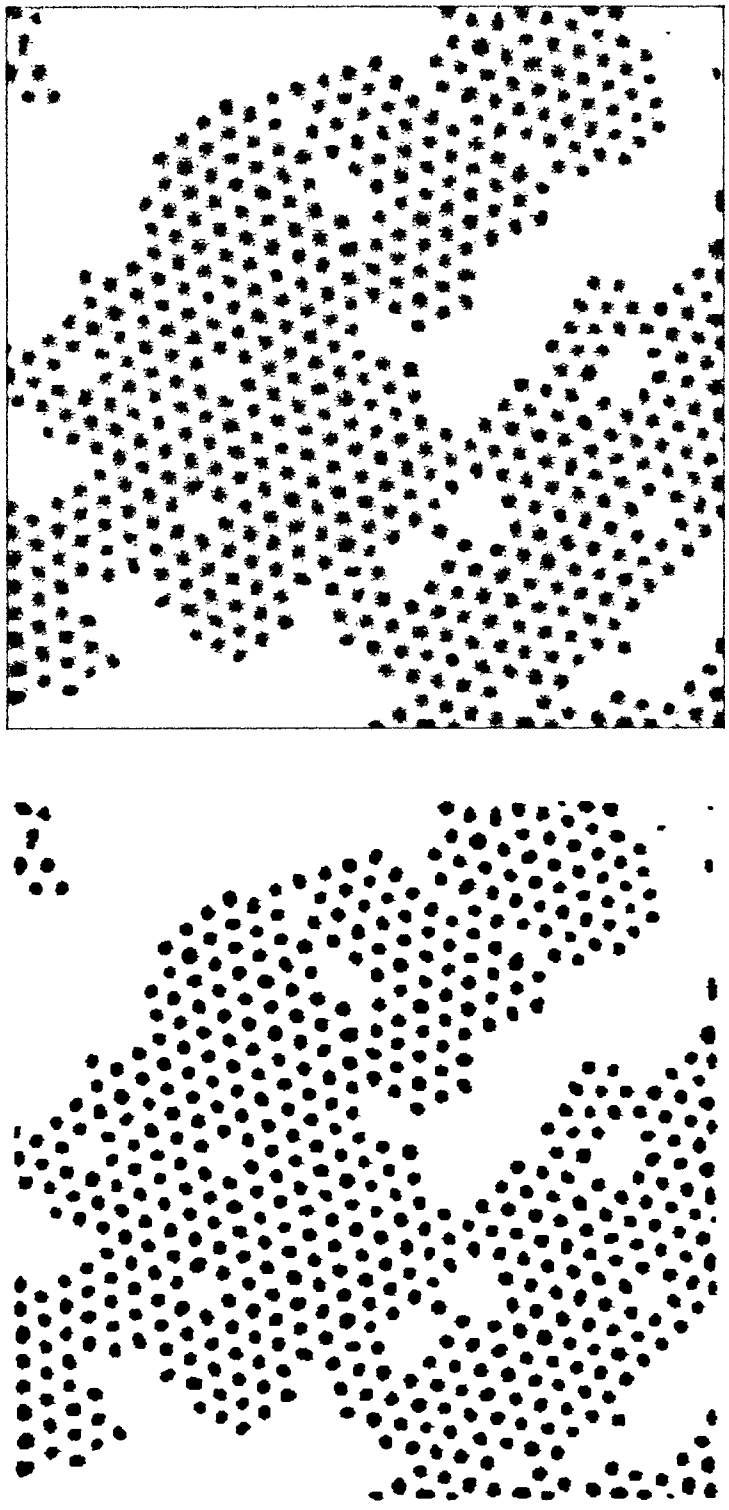

Figure 7 Martin et al

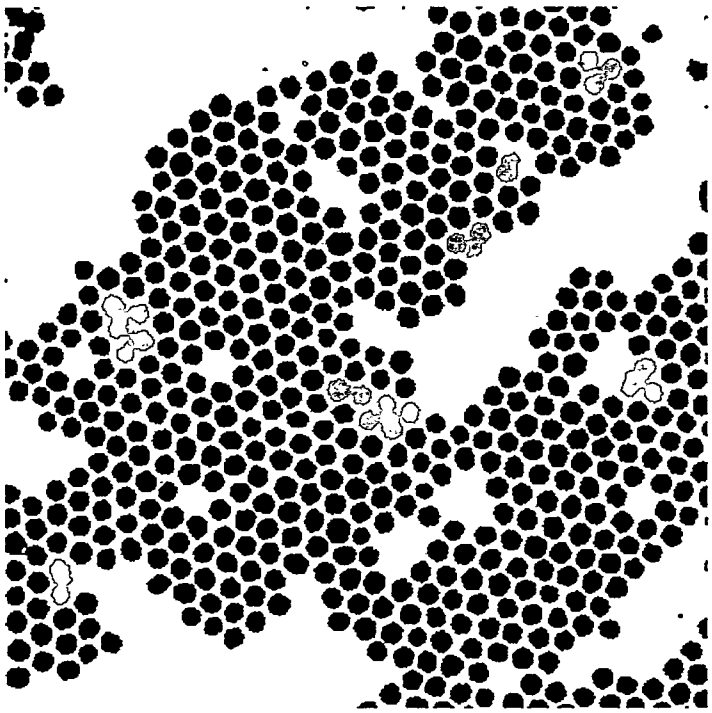

Figure 8 Martin et al

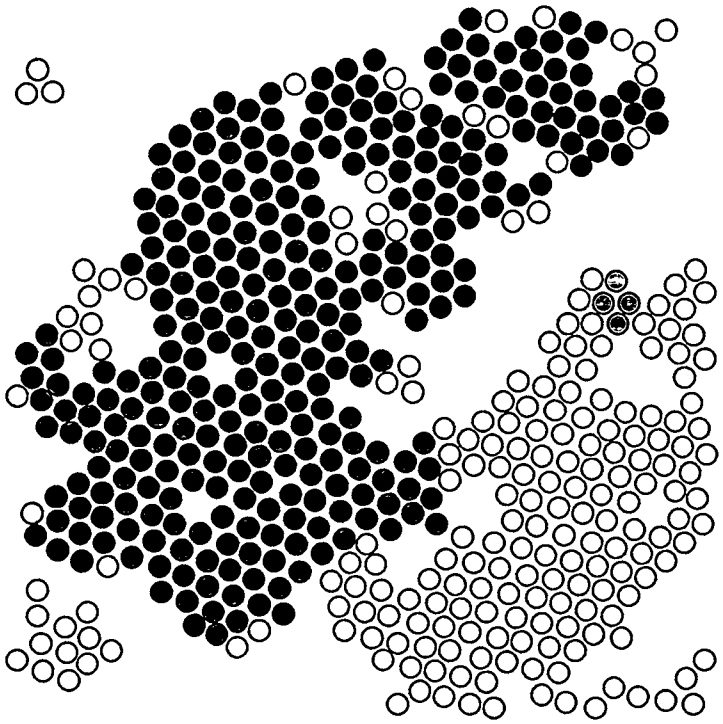

Figure 9 Martin et al

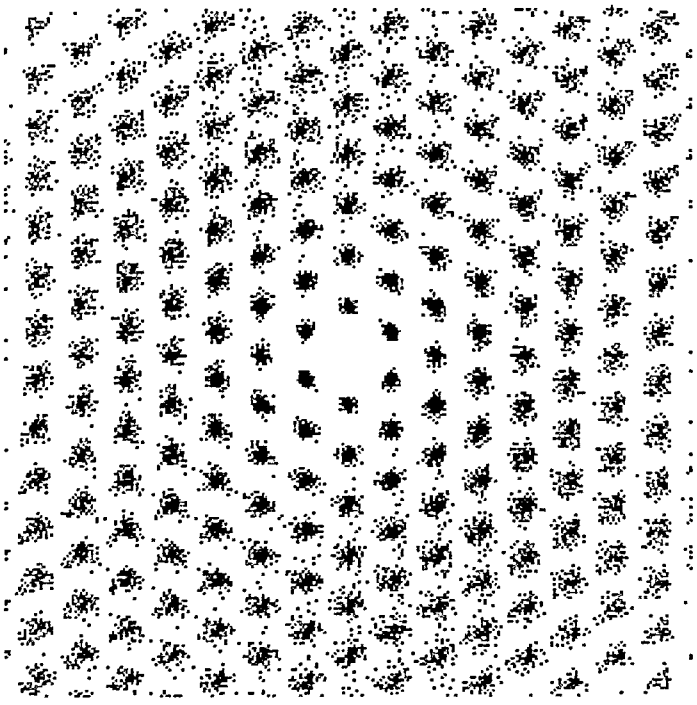

Figure 10 Martin et al

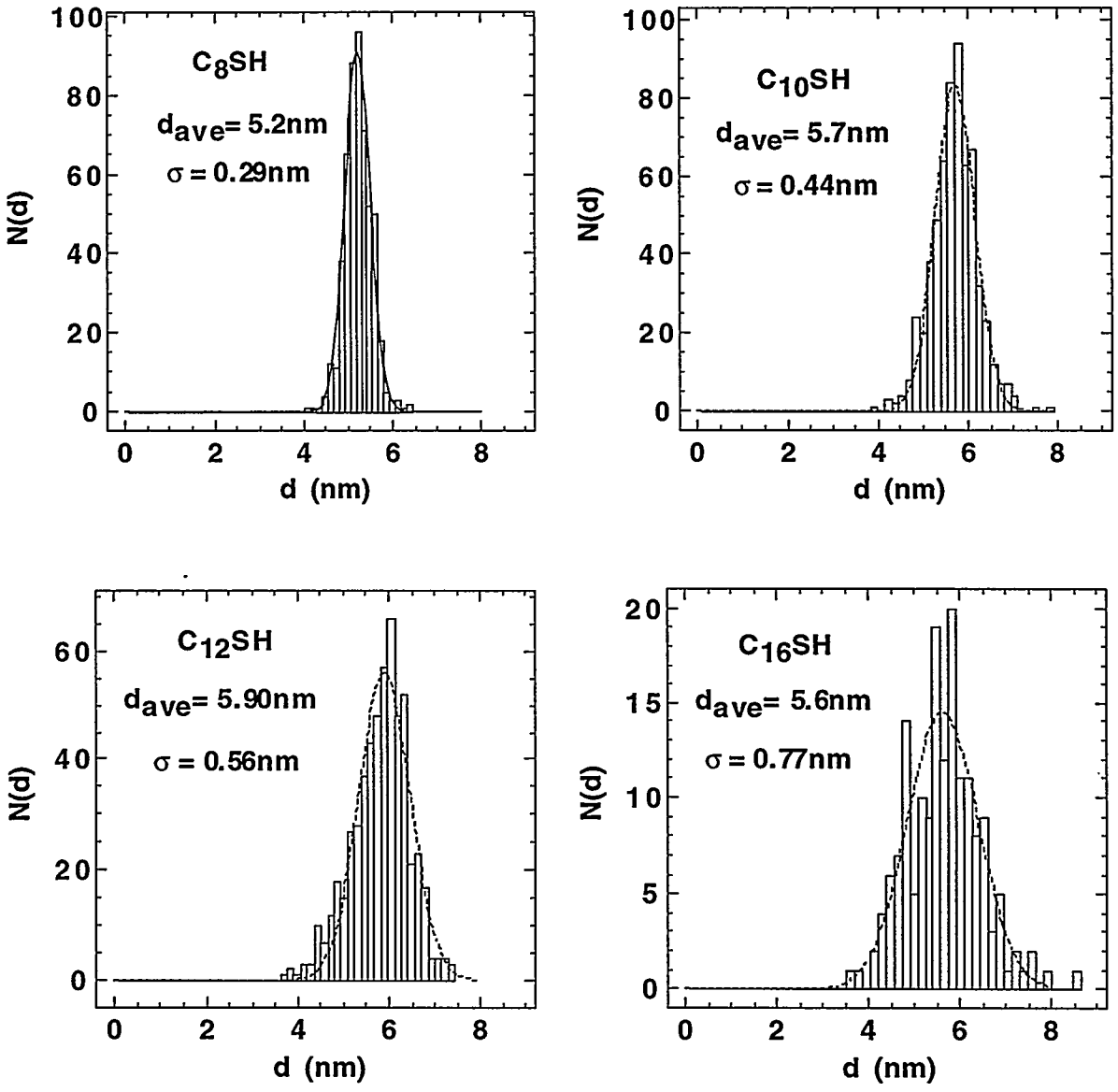

Figure 11 Martin et al

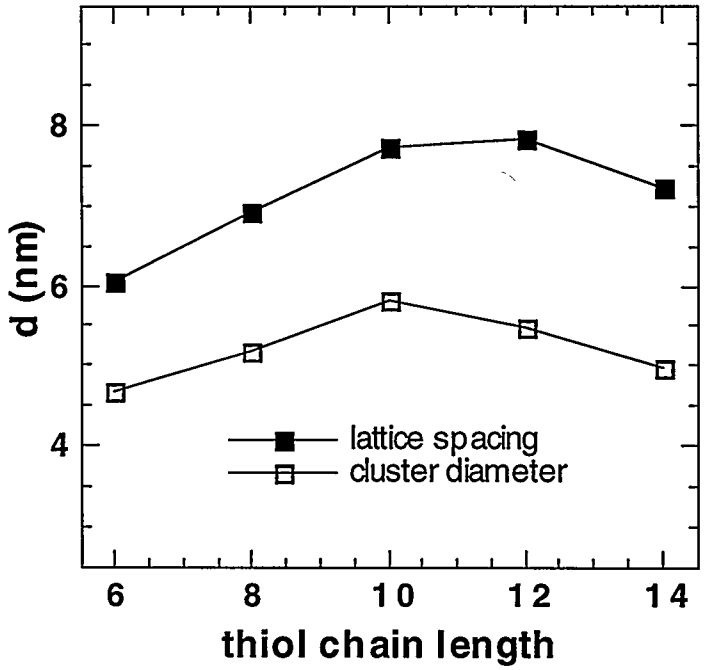

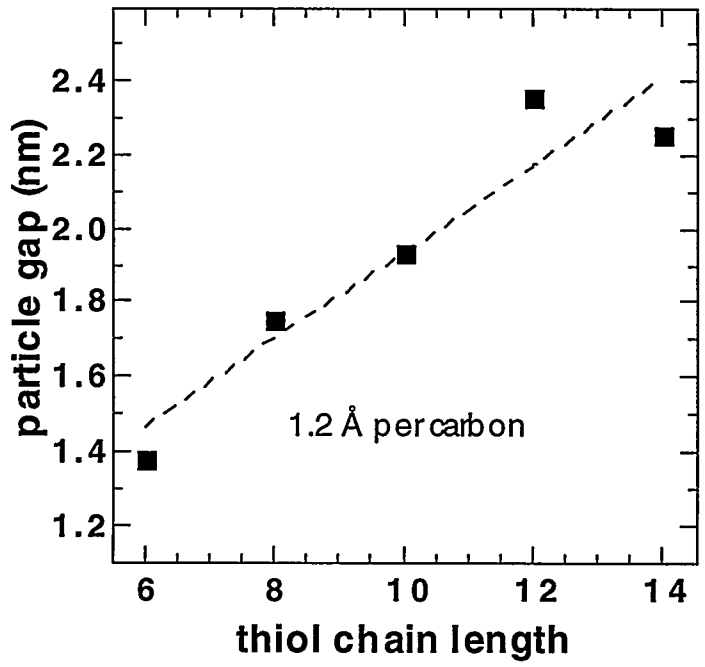

Figure 12 Martin et al

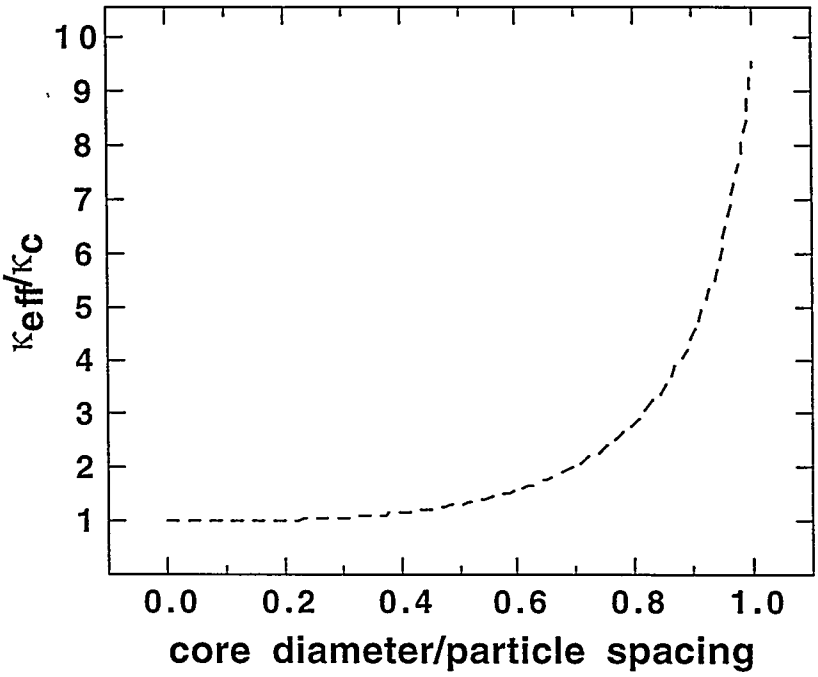

Figure 13 Martin et al